ACS NANO
Cite This: ACS Nano 2019, 13, 913−921
www.acsnano.org

ARTICLE

Waveguide-Integrated Black Phosphorus Photodetector for Mid-Infrared Applications

Li Huang,[†,‡,⊥] Bowei Dong,[†,∥,⊥] Xin Guo,[§] Yuhua Chang,[†] Nan Chen,[†] Xin Huang,[†,‡] Wugang Liao,[†,‡] Chunxiang Zhu,[†,‡] Hong Wang,[§] Chengkuo Lee,[*,†,∥] and Kah-Wee Ang[*,†,‡]

[†]Department of Electrical and Computer Engineering, National University of Singapore, 4 Engineering Drive 3, Singapore 117583
[‡]Centre for Advanced 2D Materials, National University of Singapore, 6 Science Drive 2, Singapore 117546
[§]School of Electrical and Electronic Engineering, Nanyang Technological University, 50 Nanyang Avenue, Singapore 639798
[∥]NUS Graduate School for Integrative Sciences & Engineering, National University of Singapore, 28 Medical Drive, Singapore 117456

Supporting Information

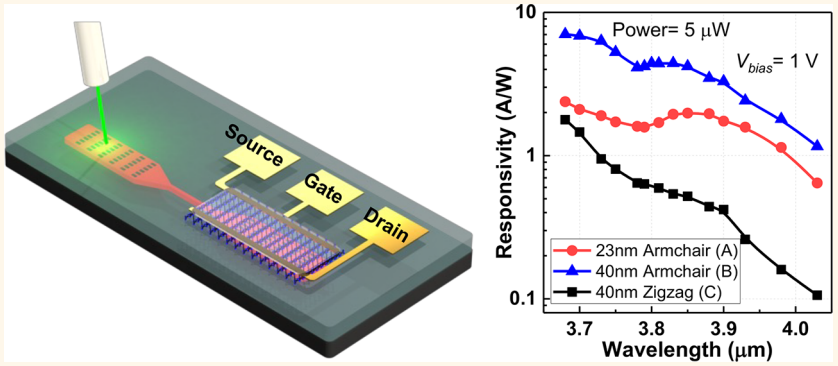

ABSTRACT: **Midinfrared (MIR), which covers numerous molecular vibrational fingerprints, has attracted enormous research interest due to its promising potential for label-free and damage-free sensing. Despite intense development efforts, the realization of waveguide-integrated on-chip sensing system has seen very limited success to date. The huge lattice mismatch between silicon and the commonly used detection materials such as HgCdTe, III−V, or II−VI compounds has been the key bottleneck that hinders their integration. Here, we realize an integration of silicon-on-insulator (SOI) waveguides with black phosphorus (BP) photodetectors. When operating near BP's cutoff wavelength where absorption is weak, the light−BP interaction is enhanced by exploiting the optical confinement in the Si waveguide and grating structure to overcome the limitation of absorption length constrained by the BP thickness. Devices with different BP crystal orientation and thickness are compared in terms of their responsivity and noise equivalent power (NEP). Spectral photoresponse from 3.68 to 4.03 μm was investigated. Additionally, power-dependent responsivity and gate-tunable photocurrent were also studied. At a bias of 1 V, the BP photodetector achieved a responsivity of 23 A/W at 3.68 μm and 2 A/W at 4 μm and a NEP less than 1 nW/Hz$^{1/2}$ at room temperature. The integration of passive Si photonics and active BP photodetector is envisaged to offer a potential pathway toward the realization of integrated on-chip systems for MIR sensing applications.**

KEYWORDS: *mid-infrared, photodetector, black phosphorus, silicon photonics, integration*

Midinfrared (MIR) beyond 3 μm is an important range of the electromagnetic spectrum that covers the atmospheric windows as well as the molecular fingerprint region.[1,2] The detection of MIR plays an important role in sensing applications such as high sensitivity greenhouse gas detection, exhaled breath monitoring, cancerous tissue identification, and water quality inspection.[3−6] Traditional infrared photodetectors commonly adopt free-space geometry, which restricts the monolithic integration with other photonic devices such as lasers and modulators. The integration of waveguide and photodetector enables miniaturization of photonic systems so as to realize chip-scale multichannel spectroscopic sensing systems with multiplexing/demultiplexing functions. Moreover, the waveguide-integrated photodetector offers another advantage of decoupling the optical absorption path from the carrier transit path and the thickness

Received: November 17, 2018
Accepted: December 26, 2018
Published: December 26, 2018

DOI: 10.1021/acsnano.8b08758
ACS Nano 2019, 13, 913−921

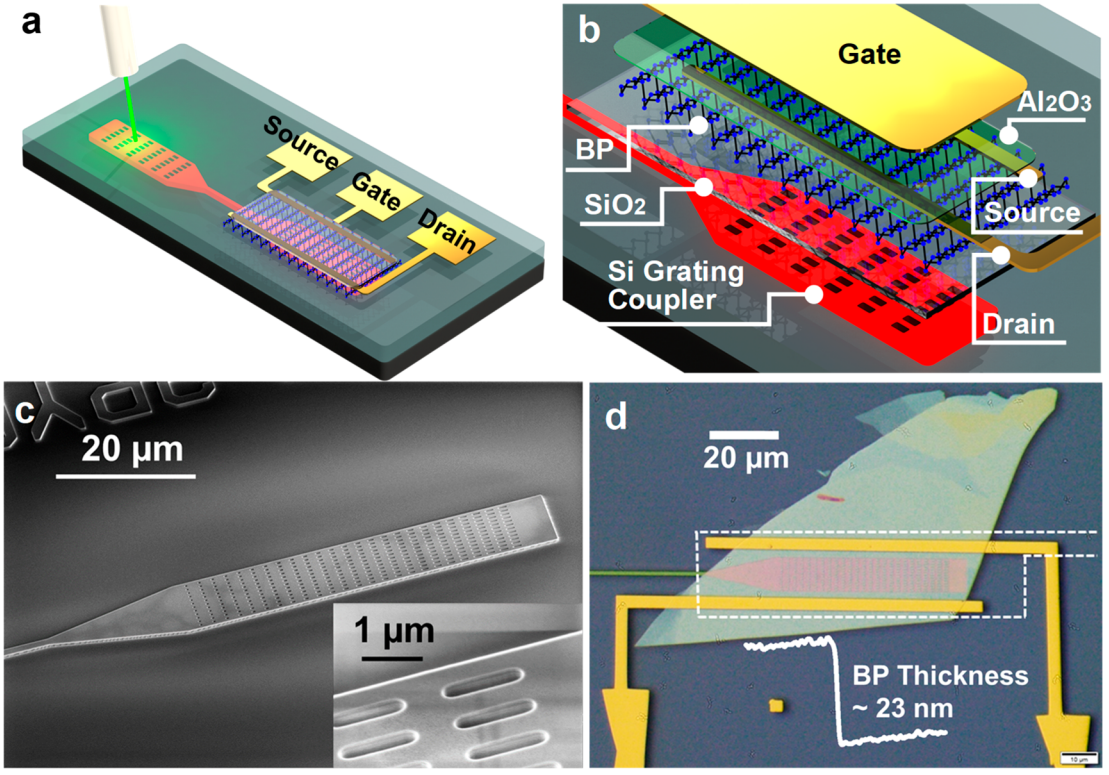

Figure 1. Device structure. (a) Schematics of the waveguide-integrated on-chip system with BP photodetector. The light is coupled into the input grating coupler from an optical fiber, transmitted through the waveguide, and coupled into the BP photodetector by the output grating coupler. (b) Zoom-in view of the output side of the device. (c) SEM image of the Si grating coupler. Inset: zoom-in image of the grating structure. (d) Microscope image of a BP photodetector on Si grating coupler before top-gate patterning. White dashed line: outline of the top gate. White solid line: AFM height profile of the 23 nm BP flake.

of the absorption material, thereby allowing more freedom in designing the device geometry for performance optimization.[7] In recent decades, waveguide-integrated photodetectors have been realized in the near-infrared (NIR) and short-wave infrared (SWIR),[7−19] benefiting from the advances in nanophotonics fabrication techniques.

Despite these developments, waveguide-integrated photodetectors have not been reported for MIR. State-of-the-art MIR photodetectors are typically based on small bandgap materials such as HgCdTe,[20] III−V,[21,22] and II−VI[23] compounds. Integrating MIR photodetectors with Si photonics faces great challenges due to the lattice mismatch between Si and these traditional MIR detection materials. As an alternative, two-dimensional (2D) material such as graphene has been proposed for MIR photodetection.[24] However, the zero-bandgap property of graphene introduces large dark current, which leads to high noise level and high power consumption. Lately rediscovered black phosphorus (BP), by virtue of its narrow direct bandgap and the layered lattice structure with in-plane anisotropy, stands out among the other candidates with its superior properties including broadband detection,[25−29] integration capability on varied substrate materials, and polarization sensitivity.[30,31] In the past few years, waveguide-integrated BP photodetectors have been demonstrated in SWIR by Li's and Hu's groups.[13−15] On the other hand, several works on MIR BP photodetectors with free-space geometry have been reported.[29,32−35] A theoretical and experimental bulk BP bandgap of ∼0.3 eV corresponds to a cutoff wavelength of 4.13 μm.[36,37] As wavelength moves into MIR beyond 3 μm and approaches BP's cutoff wavelength, photon absorption and responsivity of BP photodetectors deteriorate. Although there have been efforts targeted on extending BP's absorption edge by electric field tuning, such a device requires a cryogenic environment.[38] Consequently, realizing waveguide-integrated BP photodetectors for MIR near its cutoff wavelength at room temperature is of great importance.

Here, we demonstrate MIR waveguide-integrated BP photodetectors operating in the wavelength range from 3.68 to 4.03 μm, near BP's cutoff wavelength where absorption is considerably weak. The waveguide system not only serves as a solution for on-chip integration but also offers spatial confinement of the light to be detected and results in an enhancement of light−BP interaction compared to vertically illuminated devices. In order to explore the factors in optimizing the device performance, we first investigated the tunability offered by gate and drain bias of a BP transistor. Then devices with different BP thickness and crystal orientation with respect to the transverse direction of the waveguide were compared. To reveal their potential for weak signal detection, which is crucial for sensing applications, we investigated the power-dependent photoresponse with nanowatt to microwatt level power incident on the BP photodetector. In addition, current noise spectral density was measured to extract the noise equivalent power (NEP), which is an indication of the detection limit.

RESULTS AND DISCUSSION

Device Configuration. Figure 1a shows the schematics of the waveguide-integrated BP photodetector system which

DOI: 10.1021/acsnano.8b08758
ACS Nano 2019, 13, 913−921

consists of a grating coupler input, single mode waveguide transmission line, and a grating coupler output beneath the BP photodetector. Figure 1b shows the zoom-in details of the output side. The bottom layer includes a waveguide system with grating couplers built on a silicon-on-insulator (SOI) platform with 400 nm device layer. Waveguide insulation and passivation are realized by 200 nm planarized SiO_2 upper cladding. Detailed geometry parameters of the Si photonics are provided in Supporting Note 1. The BP flake is exfoliated from bulk crystals and transferred onto the SiO_2 cladding using a deterministic dry transfer method.[39] Source and drain electrodes are laid directly on BP along the two sides of the output grating coupler and near the active light-BP interaction area for efficient photocarrier collection. The carrier transport direction in the BP channel is perpendicular to the light propagation direction in the waveguide. The 20 nm Al_2O_3 gate dielectric separates the channel and the top electrode for gate tuning. The scanning electron microscope (SEM) image of the grating coupler is presented in Figure 1c, where its inset shows smooth sidewall and clear holes in the subwavelength grating (SWG) structure. Figure 1d shows the optical microscope image of the output side of a device before top-gate patterning. The output grating coupler and the tapered waveguide are completely covered by the light-blue BP flake. The dashed line sketches the outline of the top gate, which covers the active BP channel.

Simulation of Light Propagation and Distribution. To illustrate the light propagation and light−BP interaction in our device, we present the light field distribution using finite-difference time-domain (FDTD) simulation at a wavelength of 3.78 μm. The side view of electric field distribution overlaid with the device geometry outline is shown in Figure 2a. After being launched from the optical fiber *via* a grating coupler, the transverse electric (TE) polarized signal light is guided by the waveguide with good confinement and finally reaches the output grating coupler underneath the BP photodetector where light is directed out-of-plane and gets absorbed by the BP channel. Figure 2b shows the top view of electric field distribution of the output region in the BP plane. Figure 2c shows the cross-sectional view of electric field distribution at x = 31.25 μm, which is in a low index strip in the SWG. Field distribution at other locations in the system is presented in Figure S3. These results show the light penetrates and interacts with BP for multiple times as it propagates in the tapered waveguide and SWG. Compared with the traditional free-space coupling scheme where the absorption length is limited by transient light−matter interaction due to the inherent thin feature of 2D material, waveguide-integrated photodetector offers the advantage of enhanced light−matter interaction by guiding light in the longitudinal direction.

Photoresponse Tuned by Gate and Drain Bias. We began by investigating the photoresponse tuned by the gate bias (V_g) and drain bias (V_d) of the BP transistor. As an initial step, we measured the electrical properties of the BP transistor under dark conditions. A contour map of dark current as a function V_g and V_d is plotted in Figure 3a. The transfer curves and $I_d - V_d$ characteristics are shown in Supporting Note 2. The large drain current is located at the negative V_g and V_d regime, typifying the on-state of the p-type dominant ambipolar transistor. The transistor could be switched off with a current more than 1 order of magnitude lower than its on-current by applying a gate bias $V_g = V_0 = 2.5$ V. In the electron-conducting regime where $V_g - V_0 > 0$, the current is

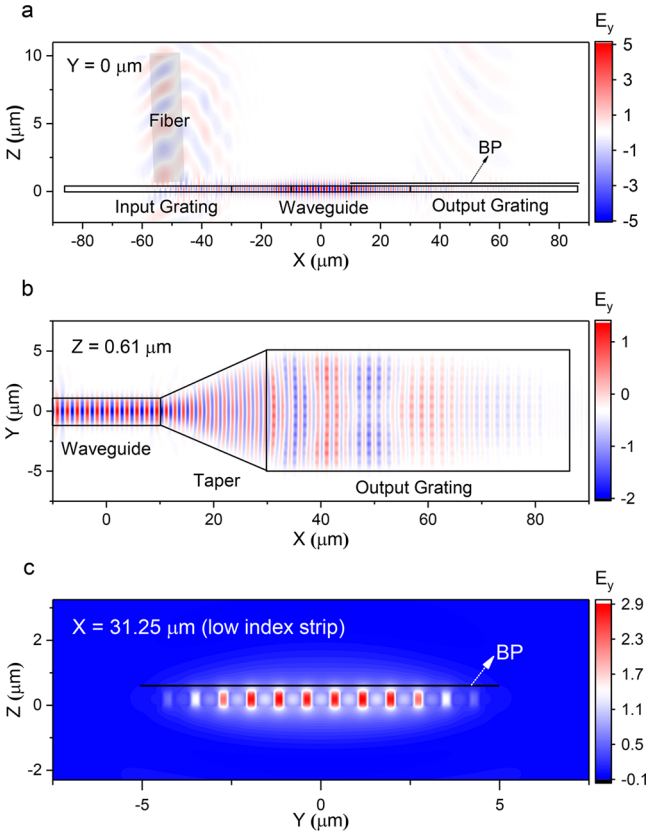

Figure 2. Finite-difference time-domain (FDTD) simulation of light propagation and distribution at 3.78 μm. (a) Side view of transverse electric field distribution in the whole system. Light from the optic fiber is coupled into the waveguide through the input grating and directed out-of-plane by the output grating for the absorption by the overlying BP. (b) Top view of the light field distribution in the BP plane. (c) Light distribution in a cross-section of the grating structure.

slightly higher than off-current and lower than hole-conducting on-current. This dark current behavior is regulated by the type, concentration, and barrier height of the carriers controlled by the gate bias and drain bias.[40] The positive V_0 indicates that the BP flake is intrinsically p-doped. With negative V_g, more holes are induced in the channel, and the transistor is turned on with a high hole-conducting current. When V_g becomes positive, holes start to get depleted as BP's Fermi level shifts away from its valence band, and finally, the current is minimized at $V_g = V_0$. Then the major carrier type is reversed from hole to electron by applying a V_g which is larger than V_0, forming an increasing electron-conducting current with larger V_g. The hole-conducting side shows higher conductance than the electron-conducting side due to higher hole mobility in BP.[41] The positive V_d side and negative V_d side are strongly asymmetric in the hole-conducting regime where $V_g < V_0$. As the metal contact is titanium, which is a low workfunction metal, on the hole-conducting side when V_g is negative, there is a large barrier for holes in the BP channel due to band bending near the contact. This hole barrier, however, could be modulated by drain bias.[42] A negative V_d lifts the energy level upward on the drain side and at the same time leads to a smaller effective gate bias of $V_g - V_d$, both of which help to reduce the band bending near drain contact, resulting in a lowered hole barrier. Therefore, I_d with negative V_d is much

DOI: 10.1021/acsnano.8b08758
ACS Nano 2019, 13, 913−921

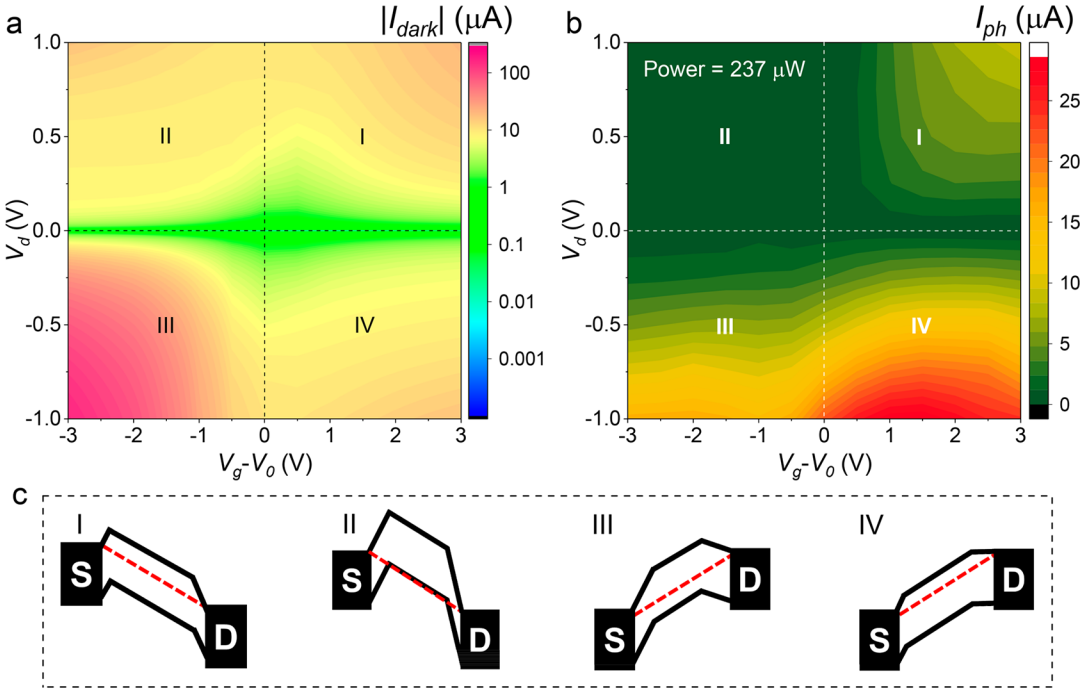

Figure 3. (a) Contour plot of the dark current *versus* gate bias and drain bias. (b) Contour plot of gate and drain-dependent photocurrent under 237 μW illumination at 3.78 μm. The optimized photocurrent is obtained with negative drain bias at the lightly n-doped region, where the hole barrier is reduced and electron traps are available for the photoconductive gain. (c) Energy band diagrams for the four quadrants labeled I, II, III, and IV in (a) and (b).

larger than I_d with positive V_d. On the electron-conducting side, because the Fermi level of titanium is very close to the bottom of BP's conduction band, there is no Schottky barrier for electrons. Therefore, for the electron-conducting regime, the polarity of V_d does not make an obvious difference in the dark current.

Based on the electrical properties of our device, we explored the photocurrent dependence on V_g and V_d under a fixed illumination power of 237 μW at a wavelength of 3.78 μm. Photocurrent is defined as the difference between the drain current under illumination and the drain current in dark conditions: $I_{ph} = |I_{d,light}| - |I_{d,dark}|$, which is the current flow formed by photogenerated electrons and holes. Photocurrent depending on gate and drain bias is presented in Figure 3b. Different from the total carrier concentration, the number of photogenerated carriers is solely determined by the illumination power, regardless of the gate bias and drain bias. Nevertheless, photocurrent is strongly dependent on the efficiency of photocarrier collection by source and drain electrodes, which is still under the control of gate bias and drain bias *via* modulation of the energy band alignment in the transistor. Furthermore, photogenerated electrons and holes are equal in number because they are induced in pairs. Considering the higher mobility of holes than electrons, photocurrent will be dominated by the collection efficiency of photogenerated holes. One of the determinants for hole collection efficiency is the hole barrier height, while another crucial factor is related to the trap-induced photoconductive gain mechanism.[43,44] Defects in the channel introduce electron trap states in BP's bandgap. These traps could capture electrons, curb electron−hole recombination, and consequently extend the lifetime of holes. Among the trap states, only those above Fermi level are empty and available for photogenerated electrons. Thus, the position of BP's Fermi level would affect the number of available trap states and further the gain in photocurrent.[29]

Figure 3c shows the energy band diagrams for the four quadrants labeled I, II, III, and IV in Figure 3a and 3b. Gate dependence of photocurrent with various negative and positive drain biases are extracted from Figure 3b and plotted in Supporting Note 3. For different drain bias, the $I_{ph} - V_g$ curve exhibits a similar trend (Figure S5a,b). On the negative side of $V_g - V_0$, BP is heavily p-doped with its energy band shifted up to align its Fermi level to titanium contact, forming a high barrier for holes traveling from BP channel to contact (Figure 3c II, III), which suppresses the conversion of photocarrier into photocurrent. As $V_g - V_0$ becomes positive, the energy band of BP shifts down, leading to a reduced hole barrier (Figure 3c I, IV). Consequently, photocurrent gradually rises as V_g increases positively and finally reaches a maximum point, after which it starts to drop as V_g moves into the heavily n-doped regime where electron traps are getting occupied and can not contribute to photoconductive gain. The $V_g - V_0$ to achieve photocurrent maximum gradually shifts positively from 1.5 to 3.5 V when drain bias increases from −1 to +1 V. Such a photocurrent maximum shift could be attributed to the need for a larger V_g to compensate for more positive V_d so as to maintain the same effective gate bias $V_g - V_d$ to obtain the maximum photocurrent. Figure S5c plots the photocurrent as a function of drain bias. At the same magnitude, negative V_d enables higher photocurrent than positive V_d as a result of hole barrier reduction by negative drain bias. In the $V_d > 0$ and $V_g - V_0 < 0$ regime, photocurrent is greatly suppressed because few photocarriers could be collected by the electrode due to the large hole barrier height. High photocurrent is obtained with V_d being negative and $V_g - V_0$ ranging from 0 to 3 V. Under such bias conditions, dark current is relatively low, hole barrier height is significantly reduced, and electron traps are available

DOI: 10.1021/acsnano.8b08758
ACS Nano 2019, 13, 913−921

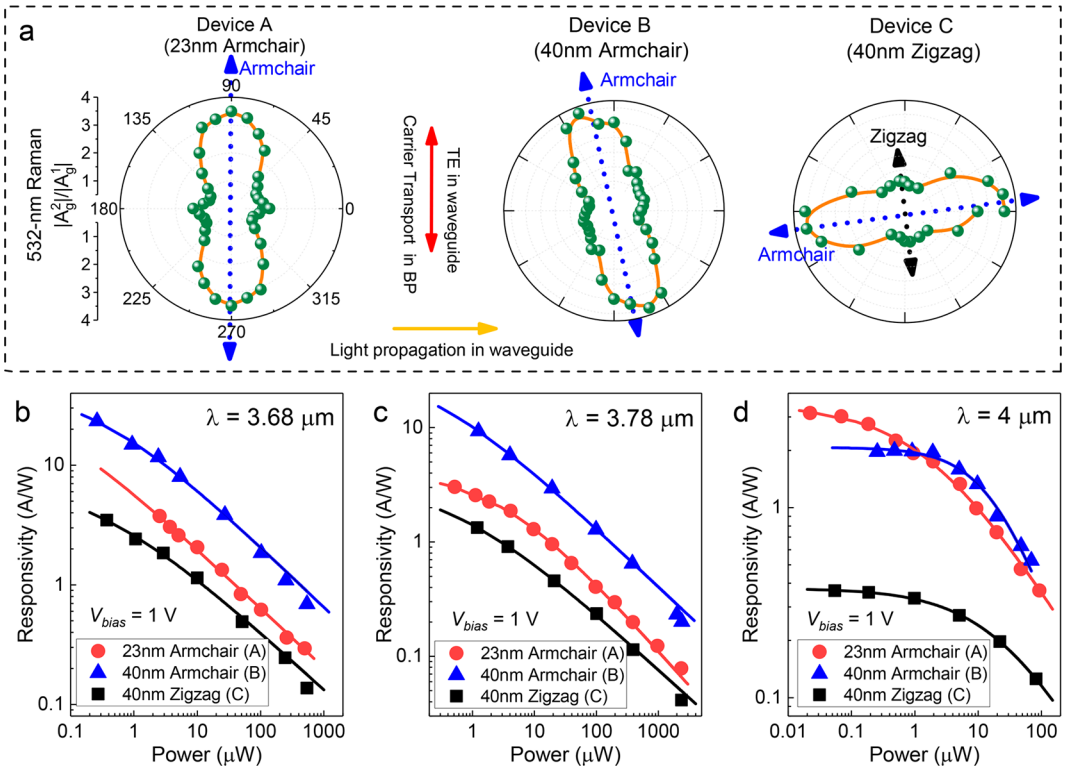

Figure 4. (a) Crystal orientation of BP identified by Raman spectroscopy in devices A, B, and C. Key: blue arrows, armchair orientation; black arrow, zigzag orientation; red arrows, carrier-transport direction in BP and transverse electric (TE) field in waveguide; yellow arrow, light propagation direction in waveguide. (b–d) Power-dependent responsivity of three devices at 3.68 (b), 3.78 (c), and 4 μm (d). Solid lines: fitting curves of responsivity by saturable photoresponse model.

for photoconductive gain. With gate and drain bias, the performance of the photodetector could be tuned to meet diverse application requirements for sensitivity and power consumption. Nevertheless, we note that the 100 nm metal may absorb and reflect most of the light once the light from the waveguide system penetrates BP and reaches the metal (Supporting Note 4). Consequently, the gate metal could severely compromise the benefit of longer BP–light interaction length brought by the waveguide system. A possible solution is to substitute the metal with few-layer graphene, which is less absorptive, or other 2D materials with larger bandgap which is transparent to MIR, or simply use a thinner metal.

BP Crystal Orientation and Thickness-Dependent Responsivity. Apart from the gate tunability, another critical factor in the integration is the alignment of BP's crystal orientation and the Si waveguide system. Light absorption and carrier mobility in BP vary with the crystal orientation due to BP's anisotropic in-plane lattice structure. For vertically incident light, strongest absorption occurs when light is polarized along the armchair direction of BP while the absorption is weakest when light polarization is parallel to BP's zigzag orientation.[30,45] Carrier mobility also maximizes along armchair direction.[41] Our Si waveguide and grating coupler are designed to support TE mode where the electric field is along the transverse direction perpendicular to the propagation direction. As a result, performance of our photodetector is dependent on the orientation of BP flake as the active layer with respect to the passive Si photonics underneath. Here, we show the results of three devices (Figure S7) with different BP crystal orientations and thicknesses. The armchair orientation of BP in both device A and B is aligned with the transverse direction in the waveguide, while the BP flake in device A is 23 nm thick and in device B is 40 nm. In device C, the armchair orientation is perpendicular to the transverse direction, while the thickness of BP is 40 nm. Polarization-resolved 532 nm Raman spectroscopy was used to determine the crystal orientation of the BP flake in our device. The three phonon peaks A_g^2, B_{2g} and A_g^1 (Figure S9) represent BP's lattice vibrational modes along the armchair, zigzag, and out-of-plane direction, respectively.[46] As the polarization filters for the incident and scattered light change, the intensity of the three peaks changes accordingly.[47,48] The ratio of A_g^2 to A_g^1 peak intensity shows a variation period of 180°, with a maximum along the armchair direction and a second maximum along the zigzag direction, which is perpendicular to the former. Figure 4a illustrates the crystal orientation in the three devices determined by Raman measurements, the direction of light propagation and transverse electric field in waveguide, and carrier transport direction in BP channel. To simplify the operation conditions, the gate was not fabricated for the three devices, and the previously used contact metal Ti was replaced by high work function metal Ni. The Fermi level of Ni is close to the top of the valence band of BP, which is conducive to forming low-resistance junctions for holes. This could largely reduce the difference of hole barrier height among the three devices due to band bending under different intrinsic doping conditions, thus making them more comparable when they are operated as photoconductors without gate.

At a fixed V_{bias} of 1 V, we measured the photocurrent of the three devices under various illumination powers at three different wavelengths (3.68, 3.78, 4 μm) and calculated the responsivity (responsivity = $\frac{I_{ph}}{power}$), as shown in Figure 4b–d.

DOI: 10.1021/acsnano.8b08758
ACS Nano 2019, 13, 913–921

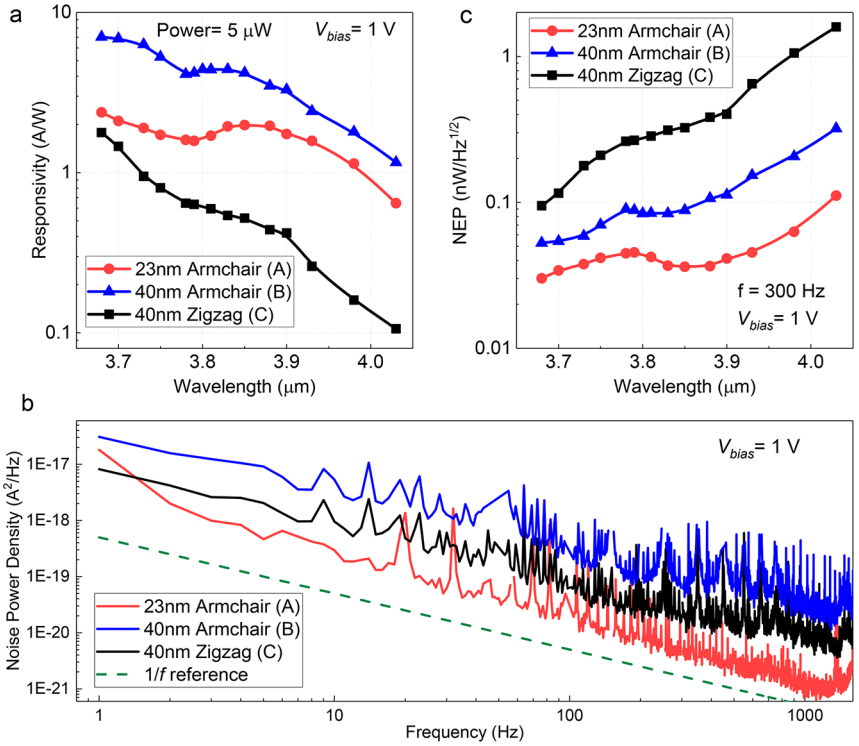

Figure 5. (a) Spectral responsivity of devices A−C. The responsivity peak between 3.8 and 3.9 μm for device A and B is possibly caused by an increase of absorption due to the subband transition when polarization of light is parallel to BP's armchair orientation. (b) Measured noise spectral density dominated by 1/f noise. (c) Spectral noise equivalent power (NEP) calculated from measured responsivity and current noise.

Device B achieved the highest responsivity benefiting from its optimal crystal orientation compared to device C and a larger BP thickness than device A. In contrast, suffering from the unfavorable crystal orientation, device C showed the lowest responsivity among the three devices despite its thicker detection material than that in device A.

Power-Dependent Photoresponse. Next, the power dependence of photoresponse was analyzed. The value of excitation power on BP was calibrated from the measured grating coupler loss at the input (Supporting Note 1) and simulated transmission at the output grating (Supporting Note 4). Under low excitation intensity, the photocurrent increases almost linearly with power (Figure S10b). However, the slope of the I_{ph} − power curve gradually becomes less steep as power increases. The sublinear relationship of I_{ph} − power is caused by more frequent photocarrier scattering and recombination at higher illumination intensity. This possibly involves two types of process. One is increased radiative recombination as excess carrier concentration gets higher when the channel is subject to high power.[49] Another process is the aforementioned trap-induced photoconductive gain. Under high excitation power, most of the electron traps are occupied with the excited electrons, so the availability of vacant electron traps, which is the source of photoconductive gain, is reduced. As a result, responsivity increases as incident power decreases, and finally saturates when power is small enough. To verify this, we fitted the measured data with a saturable photoresponse model for semiconductors with traps,[44] responsivity $= C\frac{1}{1+\left(\frac{P}{P_0}\right)^n}$, where C is a constant for a given device at a fixed wavelength, P is excitation power, P_0 is the excitation power when saturation occurs, and n is a fitting parameter. The fitted curves are plotted as solid lines in Figure 4b−d. The detailed fitting results are shown in Supporting Note 7. Although trap-induced photoconductive gain may compromise the detection speed, this may not be a critical problem in sensing applications because, unlike in telecommunications, high speed is not mandatory in most sensing scenarios where sensitivity is the major concern.

Spectral Photoresponse. According to the power-dependent responsivity for the three wavelengths 3.68, 3.78, and 4 μm in Figure 4, responsivity becomes lower at longer wavelength due to weaker light absorption by BP. To further investigate the wavelength dependence of responsivity, we measured the spectral response of the three devices under a fixed power of 5 μW. The spectral responsivity (Figure 5a) is consistent with our power dependence measurement. The overall trend is decreasing responsivity with increasing wavelength. However, there is a small but obvious peak between 3.8 and 3.9 μm in the spectral responsivity of devices A and B, while the peak is almost absent in device C. The position of this crystal orientation dependent peak in our responsivity measurements is consistent with the polarization-resolved infrared spectroscopy reported by Xia *et al.*,[30] and the peak possibly originates from an increase in photon absorption due to subband transition in BP when excitation is polarized along the armchair orientation.[50]

Current Noise and Noise Equivalent Power. Besides responsivity, another essential evaluation metric of photodetectors is noise equivalent power (NEP $= \frac{\text{current noise}}{\text{responsivity}}$), which indicates the detection limit of the detector. NEP is especially critical in sensing applications such as weak biomolecular signal detection which requires high sensitivity. Figure 5b shows the

DOI: 10.1021/acsnano.8b08758
ACS Nano 2019, 13, 913−921

measured current noise power density for devices A, B, and C. The noise spectral density of all three devices is parallel to the $1/f$ reference line, implying the noise is dominated by $1/f$ noise. At low frequency, the measured noise could be orders of magnitude higher than the shot noise calculated from dark current (Supporting Note 8). Noise level of device A is lowest among the three devices as a result of its smaller BP thickness, while device B is the noisiest due to its high dark current (Figure S11). NEP as a function of wavelength at a signal modulation frequency of 300 Hz is extracted from Figure 5a,b and plotted in Figure 5c. It is worth noting that device A achieved the lowest NEP (less than 0.12 $nW/Hz^{1/2}$), although the responsivity of device B is higher. This reveals a trade-off between responsivity and noise level when designing the thickness of detection material. Generally, thicker BP leads to higher responsivity but is simultaneously accompanied by larger dark current and higher noise level. However, in future optimizations, it is possible to overcome this trade-off by forming a heterojunction photodiode using a n-type 2D material.

CONCLUSION

In conclusion, an integrated system featuring BP photodetectors and Si photonics is demonstrated for MIR ranging from 3.68 to 4.03 μm. The waveguide and grating structure provide a platform for the light to propagate longitudinally while being coupled out-of-plane to enhance light−BP interaction. In addition, the Si waveguide offers the possibility of integrating the photodetector with other active photonic components such as lasers and modulators. Through gate and drain bias tuning, the carrier concentration, hole−barrier height, and availability of trap-induced photoconductive gain can be modulated to suppress dark current and optimize photoresponse. Furthermore, the alignment of BP crystal orientation with respect to the waveguide system is a critical factor in optimizing device performance. Optimal responsivity is obtained when the armchair orientation of BP, the carrier transport direction between the two electrodes, and the polarization of propagation mode in waveguide are aligned simultaneously. Noise spectral density indicates $1/f$ noise is dominant for frequency below 1k Hz. Responsivity of 23 A/W at 3.68 μm and 2 A/W at 4 μm and NEP less than 1 $nW/Hz^{1/2}$ were achieved with 1 V bias under room temperature. The responsivity of our devices is among the highest in the reported waveguide-integrated IR detectors (Figure S15). Our integrated system could be potentially employed in on-chip MIR sensing applications such as spectrometer sensors.

METHODS

Device Fabrication. Starting from an 8-in. SOI wafer with 220 nm Si device layer and 2 μm buried oxide (BOX) insulation layer, the Si layer was epitaxially grown to 400 nm for MIR application. A thin SiO_2 layer was deposited by plasma-enhanced chemical vapor deposition (PECVD) as the hardmask and then patterned by 248 nm deep ultraviolet (DUV) photolithography after which the pattern was transferred to the Si device layer through deep reactive-ion etching (RIE). Next, 2 μm SiO_2 was deposited by PECVD and planarized to 200 nm by chemical−mechanical planarization (CMP) to provide a flat upper cladding to integrate the BP photodetector.

BP crystals with purity ~99.998% were purchased from Smart Elements. BP flakes were first mechanically exfoliated by a tape method from bulk crystal and then transferred onto a transparent film stamp made of gel material (Gel-Pak, PF-20/17-X4). Next, a micromanipulator was used to handle a glass slide holding the stamp and to transfer the selected flake onto the SiO_2 cladding right above the output grating coupler. Source and drain electrodes were patterned by electron beam lithography (EBL) (FEI Nova NanoSEM 230) with poly(methyl methacrylate) (PMMA) as resist and isopropyl alcohol/methyl isobutyl ketone (IPA/MIBK) (1:3) as developer. Subsequently, for the first device with gate, 6 nm Ti and 100 nm Au were deposited by thermal evaporator, followed by lift-off in acetone to form the metal contacts. Gate dielectric of 20 nm Al_2O_3 was grown by atomic layer deposition (ALD) under 150 °C, after which the gate electrode was fabricated by the same method as source and drain. For devices A−C, the crystal orientation of BP was determined by Raman spectroscopy immediately after BP exfoliation and transfer onto the gel stamp, the source/drain electrodes were 6 nm Ni and 80 nm Au deposited by sputtering, and the fabrication ended with 20 nm alumina passivation by ALD without the last step of gate electrode deposition.

Material, Electrical, and Photoresponse Characterization. Raman spectroscopy was measured by a WITec Alpha 300R with a 532 nm laser. During the polarization-resolved measurement, the polarizers for incident and reflected light were kept parallel. The thickness of BP was measured by AFM (Bruker). Keithley 2401 source meters were used to apply drain and gate bias and measure drain current. A continuous wave laser (Daylight Solutions Inc., TLS-41038) was launched into an optic fiber (Thorlabs, P3-23Z-FC-2) by an MIR lens and aligned to the input grating coupler with a six-axis micromanipulator at an incident angle of 11°. The intensity of the laser output was calibrated with a power meter (Newport, 843-R), a thermopile sensor (Newport, 919P-003-10) and a mid-infrared InSb detector (Horiba DSS-IS020L). A low-noise current preamplifier (Stanford Research System, SR570), a dynamic signal analyzer (Hewlett-Packard, 35670A), and a parameter analyzer (Agilent 4155B) were used to measure the noise spectral density. The measurement setups are illustrated in Supporting Note 9. Samples were taken at ambient and at room temperature during the measurements.

ASSOCIATED CONTENT

Supporting Information

The Supporting Information is available free of charge on the ACS Publications website at DOI: 10.1021/acsnano.8b08758.

Supporting Notes 1−10 describing design and simulation, experimental results, characterization data, and measurement setups (PDF)

AUTHOR INFORMATION

Corresponding Authors

*E-mail: eleakw@nus.edu.sg.

*E-mail: elelc@nus.edu.sg.

ORCID

Li Huang: 0000-0002-2188-3178

Xin Huang: 0000-0003-2065-6384

Wugang Liao: 0000-0002-1461-2222

Chunxiang Zhu: 0000-0002-6548-5366

Chengkuo Lee: 0000-0002-8886-3649

Kah-Wee Ang: 0000-0003-1919-3351

Author Contributions

⊥L.H. and B.D. contributed equally. K.-W.A. and C.L. supervised the project. L.H. and B.D. carried out the device fabrication and characterization. X.G. and H.W. provided the photoresponse measurement setup. B.D. and N.C. performed the Si photonics simulation. L.H., Y.C., and X.H. performed the material characterization. W.L. performed the noise spectral density measurement. L.H. and B.D. drafted the manuscript.

DOI: 10.1021/acsnano.8b08758
ACS Nano 2019, 13, 913−921

Funding

This research is supported by the A*STAR Science and Engineering Research Council Grant (No. 152-70-00013), the National Research Foundation Competitive Research Programs (NRF-CRP15-2015-01 and NRF-CRP15-2015-02), and the National Research Foundation, Prime Minister's Office, Singapore, under its medium-sized center program.

Notes

The authors declare no competing financial interest.

REFERENCES

(1) Jackson, S. D. Towards High-Power Mid-Infrared Emission from A Fibre Laser. *Nat. Photonics* **2012**, *6*, 423−431.
(2) Beck, M.; Hofstetter, D.; Aellen, T.; Faist, J.; Oesterle, U.; Llegems, M.; Gini, E.; Melchior, H. Continuous Wave Operation of A Mid-Infrared Semiconductor Laser at Room Temperature. *Science* **2002**, *295*, 301−305.
(3) Chen, Y.; Lin, H.; Hu, J.; Li, M. Heterogeneously Integrated Silicon Photonics for the Mid-infrared and Spectroscopic Sensing. *ACS Nano* **2014**, *8*, 6955−6961.
(4) Dam, J. S.; Tidemand-Lichtenberg, P.; Pedersen, C. Room-Temperature Mid-Infrared Single-Photon Spectral Imaging. *Nat. Photonics* **2012**, *6*, 788−793.
(5) Thamer, M.; De Marco, L.; Ramasesha, K.; Mandal, A.; Tokmakoff, A. Ultrafast 2D IR Spectroscopy of the Excess Proton in Liquid Water. *Science* **2015**, *350*, 78−82.
(6) Rodrigo, D.; Limaj, O.; Janner, D.; Etezadi, D.; Garcia de Abajo, F. J.; Pruneri, V.; Altug, H. Mid-Infrared Plasmonic Biosensing with Graphene. *Science* **2015**, *349*, 165−168.
(7) Yin, T.; Cohen, R.; Morse, M. M.; Sarid, G.; Chetrit, Y.; Rubin, D.; Paniccia, M. J. 31 GHz Ge n-i-p Waveguide Photodetectors on Silicon-on-Insulator Substrate. *Opt. Express* **2007**, *15*, 13965−13971.
(8) Pearsall, T. P.; Temkin, H.; Bean, J. C.; Luryi, S. Avalanche Gain in Ge_xSi_{1-x}/Si Infrared Waveguide Detectors. *IEEE Electron Device Lett.* **1986**, *7*, 330−332.
(9) Sheng, Z.; Liu, L.; Brouckaert, J.; He, S.; Van Thourhout, D. InGaAs PIN Photodetectors Integrated on Silicon-on-Insulator Waveguides. *Opt. Express* **2010**, *18*, 1756−1761.
(10) Ackert, J. J.; Thomson, D. J.; Shen, L.; Peacock, A. C.; Jessop, P. E.; Reed, G. T.; Mashanovich, G. Z.; Knights, A. P. High-Speed Detection at Two Micrometres with Monolithic Silicon Photodiodes. *Nat. Photonics* **2015**, *9*, 393−396.
(11) Grote, R. R.; Souhan, B.; Ophir, N.; Driscoll, J. B.; Bergman, K.; Bahkru, H.; Green, W. M. J.; Osgood, R. M. Extrinsic Photodiodes for Integrated Mid-Infrared Silicon Photonics. *Optica* **2014**, *1*, 264−267.
(12) Bie, Y. Q.; Grosso, G.; Heuck, M.; Furchi, M. M.; Cao, Y.; Zheng, J.; Bunandar, D.; Navarro-Moratalla, E.; Zhou, L.; Efetov, D. K.; Taniguchi, T.; Watanabe, K.; Kong, J.; Englund, D.; Jarillo-Herrero, P. A $MoTe_2$-Based Light-Emitting Diode and Photodetector for Silicon Photonic Integrated Circuits. *Nat. Nanotechnol.* **2017**, *12*, 1124−1129.
(13) Youngblood, N.; Chen, C.; Koester, S. J.; Li, M. Waveguide-Integrated Black Phosphorus Photodetector with High Responsivity and Low Dark Current. *Nat. Photonics* **2015**, *9*, 247−252.
(14) Chen, C.; Youngblood, N.; Peng, R.; Yoo, D.; Mohr, D. A.; Johnson, T. W.; Oh, S.-H.; Li, M. Three-Dimensional Integration of Black Phosphorus Photodetector with Silicon Photonics and Nanoplasmonics. *Nano Lett.* **2017**, *17*, 985−991.
(15) Deckoff-Jones, S.; Lin, H.; Kita, D.; Zheng, H.; Li, D.; Zhang, W.; Hu, J. Chalcogenide Glass Waveguide-Integrated Black Phosphorus Mid-Infrared Photodetectors. *J. Opt.* **2018**, *20*, No. 044004.
(16) Wang, X.; Cheng, Z.; Xu, K.; Tsang, H. K.; Xu, J.-B. High-Responsivity Graphene/Silicon-Heterostructure Waveguide Photodetectors. *Nat. Photonics* **2013**, *7*, 888−891.
(17) Gan, X.; Shiue, R.-J.; Gao, Y.; Meric, I.; Heinz, T. F.; Shepard, K.; Hone, J.; Assefa, S.; Englund, D. Chip-Integrated Ultrafast Graphene Photodetector with High Responsivity. *Nat. Photonics* **2013**, *7*, 883−887.
(18) Wang, R.; Sprengel, S.; Muneeb, M.; Boehm, G.; Baets, R.; Amann, M.-C.; Roelkens, G. 2 μm Wavelength Range InP-Based Type-II Quantum Well Photodiodes Heterogeneously Integrated on Silicon Photonic Integrated Circuits. *Opt. Express* **2015**, *23*, 26834−26841.
(19) Gassenq, A.; Hattasan, N.; Cerutti, L.; Rodriguez, J. B.; Tournie, E.; Roelkens, G. Study of Evanescently-Coupled and Grating-Assisted GaInAsSb Photodiodes Integrated on A Silicon Photonic Chip. *Opt. Express* **2012**, *20*, 11665−11672.
(20) Keuleyan, S.; Lhuillier, E.; Brajuskovic, V.; Guyot-Sionnest, P. Mid-Infrared HgTe Colloidal Quantum Dot Photodetectors. *Nat. Photonics* **2011**, *5*, 489−493.
(21) Chang, C. C.; Sharma, Y. D.; Kim, Y. − S.; Bur, J. A.; Shenoi, R. V.; Krishna, S.; Huang, D.; Lin, S. − Y. A Surface Plasmon Enhanced Infrared Photodetector Based on InAs Quantum Dots. *Nano Lett.* **2010**, *10*, 1704−1709.
(22) Jia, B. W.; Tan, K. H.; Loke, W. K.; Wicaksono, S.; Lee, K. H.; Yoon, S. F. Monolithic Integration of InSb Photodetector on Silicon for Mid-Infrared Silicon Photonics. *ACS Photonics* **2018**, *5*, 1512−1520.
(23) Singh, V.; Lin, P. T.; Patel, N.; Lin, H.; Li, L.; Zou, Y.; Deng, F.; Ni, C.; Hu, J.; Giammarco, J.; Soliani, A. P.; Zdyrko, B.; Luzinov, I.; Novak, S.; Novak, J.; Wachtel, P.; Danto, S.; Musgraves, J. D.; Richardson, K.; Kimerling, L. C.; et al. Mid-Infrared Materials and Devices on A Si Platform for Optical Sensing. *Sci. Technol. Adv. Mater.* **2014**, *15*, No. 014603.
(24) Yao, Y.; Shankar, R.; Rauter, P.; Song, Y.; Kong, J.; Loncar, M.; Capasso, F. High-Responsivity Mid-Infrared Graphene Detectors with Antenna-Enhanced Photocarrier Generation and Collection. *Nano Lett.* **2014**, *14*, 3749−3754.
(25) Wu, J.; Koon, G. K. W.; Xiang, D.; Han, C.; Toh, C. T.; Kulkarni, E. S.; Verzhbitskiy, I.; Carvalho, A.; Rodin, A. S.; Koenig, S. P.; Eda, G.; Chen, W.; Neto, A. H.; Ozyilmaz, B. Colossal Ultraviolet Photoresponsivity of Few-Layer Black Phosphorus. *ACS Nano* **2015**, *9*, 8070−8077.
(26) Buscema, M.; Groenendijk, D. J.; Blanter, S. I.; Steele, G. A.; van der Zant, H. S. J.; Castellanos-Gomez, A. Fast and Broadband Photoresponse of Few-Layer Black Phosphorus Field-Effect Transistors. *Nano Lett.* **2014**, *14*, 3347−3352.
(27) Engel, M.; Steiner, M.; Avouris, P. Black Phosphorus Photodetector for Multispectral, High-Resolution Imaging. *Nano Lett.* **2014**, *14*, 6414−6417.
(28) Huang, L.; Tan, W. C.; Wang, L.; Dong, B.; Lee, C.; Ang, K. − W. Infrared Black Phosphorus Phototransistor with Tunable Responsivity and Low Noise Equivalent Power. *ACS Appl. Mater. Interfaces* **2017**, *9*, 36130−36136.
(29) Guo, Q.; Pospischil, A.; Bhuiyan, M.; Jiang, H.; Tian, H.; Farmer, D.; Deng, B.; Li, C.; Han, S. − J.; Wang, H.; Xia, Q.; Ma, T. P.; Mueller, T.; Xia, F. Black Phosphorus Mid-Infrared Photodetectors with High Gain. *Nano Lett.* **2016**, *16*, 4648−4655.
(30) Xia, F.; Wang, H.; Jia, Y. Rediscovering Black Phosphorus as an Anisotropic Layered Material for Optoelectronics and Electronics. *Nat. Commun.* **2014**, *5*, 4458.
(31) Ling, X.; Wang, H.; Huang, S.; Xia, F.; Dresselhaus, M. S. The Renaissance of Black Phosphorus. *Proc. Natl. Acad. Sci. U. S. A.* **2015**, *112*, 4523−4530.
(32) Xu, M.; Gu, Y.; Peng, R.; Youngblood, N.; Li, M. Black Phosphorus Mid-Infrared Photodetectors. *Appl. Phys. B: Lasers Opt.* **2017**, *123*, 130.
(33) Suess, R. J.; Leong, E.; Garrett, J. L.; Zhou, T.; Salem, R.; Munday, J. N.; Murphy, T. E.; Mittendorff, M. Mid-Infrared Time-Resolved Photoconduction in Black Phosphorus. *2D Mater.* **2016**, *3*, No. 041006.
(34) Amani, M.; Regan, E.; Bullock, J.; Ahn, G. H.; Javey, A. Mid-Wave Infrared Photoconductors Based on Black Phosphorus-Arsenic Alloys. *ACS Nano* **2017**, *11*, 11724−11731.

DOI: 10.1021/acsnano.8b08758
ACS Nano 2019, 13, 913−921

(35) Bullock, J.; Amani, M.; Cho, J.; Chen, Y. Z.; Ahn, G. H.; Adinolfi, V.; Shrestha, V. R.; Gao, Y.; Crozier, K. B.; Chueh, Y. L.; Javey, A. Polarization-Resolved Black Phosphorus/Molybdenum Disulfide Mid-Wave Infrared Photodiodes with High Detectivity at Room Temperature. *Nat. Photonics* **2018**, *12*, 601.
(36) Tran, V.; Soklaski, R.; Liang, Y.; Yang, L. Layer-Controlled Band Gap and Anisotropic Excitons in Few-Layer Black Phosphorus. *Phys. Rev. B: Condens. Matter Mater. Phys.* **2014**, *89*, 235319.
(37) Keyes, R. W. The Electrical Properties of Black Phosphorus. *Phys. Rev.* **1953**, *92*, 580−584.
(38) Chen, X.; Lu, X.; Deng, B.; Sinai, O.; Shao, Y.; Li, C.; Yuan, S.; Tran, V.; Watanabe, K.; Taniguchi, T.; Naveh, D.; Yang, L.; Xia, F. Widely Tunable Black Phosphorus Mid-Infrared Photodetector. *Nat. Commun.* **2017**, *8*, 1672.
(39) Castellanos-Gomez, A.; Buscema, M.; Molenaar, R.; Singh, V.; Janssen, L.; van der Zant, H. S. J.; Steele, G. A. Deterministic Transfer of Two-Dimensional Materials by All-Dry Viscoelastic Stamping. *2D Mater.* **2014**, *1*, No. 011002.
(40) Penumatcha, A. V.; Salazar, R. B.; Appenzeller, J. Analysing Black Phosphorus Transistors Using An Analytic Schottky Barrier MOSFET Model. *Nat. Commun.* **2015**, *6*, 8948.
(41) Qiao, J.; Kong, X.; Hu, Z. X.; Yang, F.; Ji, W. High-Mobility Transport Anisotropy and Linear Dichroism in Few-Layer Black Phosphorus. *Nat. Commun.* **2014**, *5*, 4475.
(42) Du, Y.; Liu, H.; Deng, Y.; Ye, P. D. Device Perspective for Black Phosphorus Field-Effect Transistors: Contact Resistance, Ambipolar Behavior, and Scaling. *ACS Nano* **2014**, *8*, 10035−10042.
(43) Soci, C.; Zhang, A.; Bao, X.-Y.; Kim, H.; Lo, Y.-H.; Wang, D. Nanowire Photodetectors. *J. Nanosci. Nanotechnol.* **2010**, *10*, 1430−1449.
(44) Soci, C.; Zhang, A.; Xiang, B.; Dayeh, S. A.; Aplin, D. P. R.; Park, J.; Bao, X.-Y.; Lo, Y. − H.; Wang, D. ZnO Nanowire UV Photodetectors with High Internal Gain. *Nano Lett.* **2007**, *7*, 1003−1009.
(45) Low, T.; Rodin, A. S.; Carvalho, A.; Jiang, Y.; Wang, H.; Xia, F.; Castro Neto, A. H. Tunable Optical Properties of Multilayer Black Phosphorus Thin Films. *Phys. Rev. B: Condens. Matter Mater. Phys.* **2014**, *90*, No. 075434.
(46) Fei, R.; Yang, L. Lattice Vibrational Modes and Raman Scattering Spectra of Strained Phosphorene. *Appl. Phys. Lett.* **2014**, *105*, No. 083120.
(47) Ling, X.; Huang, S.; Hasdeo, E. H.; Liang, L.; Parkin, W. M.; Tatsumi, Y.; Nugraha, A. R. T.; Puretzky, A. A.; Das, P. M.; Sumpter, B. G.; Geohegan, D. B.; Kong, J.; Saito, R.; Drndic, M.; Meunier, V.; Dresselhaus, M. S. Anisotropic Electron-Photon and Electron-Phonon Interactions in Black Phosphorus. *Nano Lett.* **2016**, *16*, 2260−2267.
(48) Ribeiro, H. B.; Pimenta, M. A.; de Matos, C. J. S.; Moreira, R. L.; Rodin, A. S.; Zapata, J. D.; de Souza, E. A. T.; Castro Neto, A. H. Unusual Angular Dependence of the Raman Response in Black Phosphorus. *ACS Nano* **2015**, *9*, 4270−4276.
(49) Surrente, A.; Mitioglu, A. A.; Galkowski, K.; Klopotowski, L.; Tabis, W.; Vignolle, B.; Maude, D. K.; Plochocka, P. Onset of Exciton-Exciton Annihilation in Single-Layer Black Phosphorus. *Phys. Rev. B: Condens. Matter Mater. Phys.* **2016**, *94*, No. 075425.
(50) Zhang, G.; Huang, S.; Chaves, A.; Song, C.; Özçelik, V. O.; Low, T.; Yan, H. Infrared Fingerprints of Few-Layer Black Phosphorus. *Nat. Commun.* **2017**, *8*, 14071.

DOI: 10.1021/acsnano.8b08758
ACS Nano 2019, 13, 913−921